



# Microstructural Features and Mechanical Integrity of Wire Arc Additive Manufactured SS321/Inconel 625 Functionally Gradient Material

S. Mohan Kumar, A. Rajesh Kannan, N. Pravin Kumar, R. Pramod, N. Siva Shanmugam, A.S. Vishnu, and S.G. Channabasavanna

Submitted: 25 June 2020 / Revised: 1 February 2021 / Accepted: 18 February 2021 / Published online: 17 March 2021

The additively fabricated functionally gradient structures can be a potential replacement for conventionally manufactured structures via fusion welding techniques. A SS321/Inconel 625 functionally gradient material was processed by wire arc additive manufacturing (WAAM) process. The WAAM-formed SS321 comprises of equiaxed and columnar structures, while the Inconel 625 consists of dendritic structures. It can be concluded that a very narrow interface was formed between the additively manufactured SS321/Inconel 625 FGM without forming cracks or fissures. Energy-dispersive x-ray spectroscopy (EDS) element maps show a smooth transition of elements at the interface without much segregation while EDS point scan confirmed the presence of laves phase. The electron backscatter diffraction results at the interface region revealed continuous crystallographic growth with large elongated grains in the  $\langle 001 \rangle$  orientation. Tensile properties were better for SS321 and comparable for Inconel 625 than the wrought alloys, while the interface FGM sample failed on the SS321 side. The micro-hardness steadily changed from 226–195 HV and 272–236 HV in SS321 and Inconel 625, respectively. The WAAM process demonstrates that successful FGM components can be fabricated with multi-material and controlled properties.

**Keywords** functionally gradient material, mechanical properties, microstructure, nickel-based superalloy, stainless steel, wire arc additive manufacturing

## 1. Introduction

WAAM is a developing and attractive metal additive manufacturing technique that uses electric arc as the heat source and filler wires as the deposition material to manufacture medium and large scale structures via layer-by-layer process (Ref 1). WAAM process has been efficiently employed in fabricating structures with many alloys such as aluminum, nickel, titanium and steel (Ref 2–4). The weldability is the significant factor which controls the production of a metallic structure by WAAM, as this method is based on the application of successive layers of weld beads on top of each other. Functional Graded Materials (FGMs) are a novel developing class of high-strength materials that are very suitable for a wide range of industrial applications as they allow different functional performances within one part (Ref 5). Conventionally, these FGMs are manufactured through post-processing with fusion welding techniques, diffusion bonding, or friction stir welding (Ref 6, 7). SS321 and Inconel 625 are widely used

alloys to fabricate bi-metallic structures for aerospace, power generation, gas turbines, high-temperature bolts, petrochemical, and marine applications because of their exceptional corrosion performance and mechanical properties at temperatures below 850 °C (Ref 8–10). For the above-said applications, fusion welding techniques are employed to weld dissimilar alloys. However, welding dissimilar alloys will locally alter the microchemistry and can cause higher amount of distortion as a result of the difference in the thermal expansion coefficient. Also, brittle secondary phases formation reduces the mechanical properties, and in some cases, stress-corrosion cracking is noticed (Ref 11). Nickel-based superalloys such as Inconel 625 are hard to machine due to their lower thermal conductivity, higher hardness, and higher work hardening index (Ref 12). Near-net-shaped components produced through additive manufacturing can considerably reduce the machining time and is a promising manufacturing technology for fabricating multi-material structures. Furthermore, the recent advancements in WAAM technology have increased the possibilities of fabricating bi-metallic components.

Manufacturing FGM using WAAM process has the possibility to realize new materials in an accelerated manner as a result of different compositions and mechanical properties (Ref 13). According to Chandrasekaran et al. (Ref 14) FGMs are mainly classified into two types namely continuously varying and step-wise varying FGM. Most of the FGMs fabricated were through powder metallurgy technique and the compositional gradient was easily achieved. Bobbio et al. (Ref 15) fabricated FGM using Ti-6Al-4V to Invar and examined the microstructural features, phases, and microhardness. In addition, they observed cracks in the interface and are attributed to the formation of intermetallic phases such as FeTi, Fe<sub>2</sub>Ti, NiTi<sub>2</sub>, and Ni<sub>3</sub>Ti. Chen et al (Ref 16) developed an FGM of 316L/Inconel625 by laser direct metal deposition and observed columnar dendritic growth with the presence of laves phase.

S. Mohan Kumar, A. Rajesh Kannan, N. Pravin Kumar, R. Pramod, and N. Siva Shanmugam, Department of Mechanical Engineering, National Institute of Technology, Tiruchirappalli, Tamil Nadu, India; A.S. Vishnu, Department of Mechanical and Aerospace Engineering, Indian Institute of Technology, Hyderabad, Telangana, India; and S.G. Channabasavanna, Department of Mechanical Engineering, Maharaja Institute of Technology, Thandavapura, Karnataka, India. Contact e-mail: nsiva@nitt.edu.

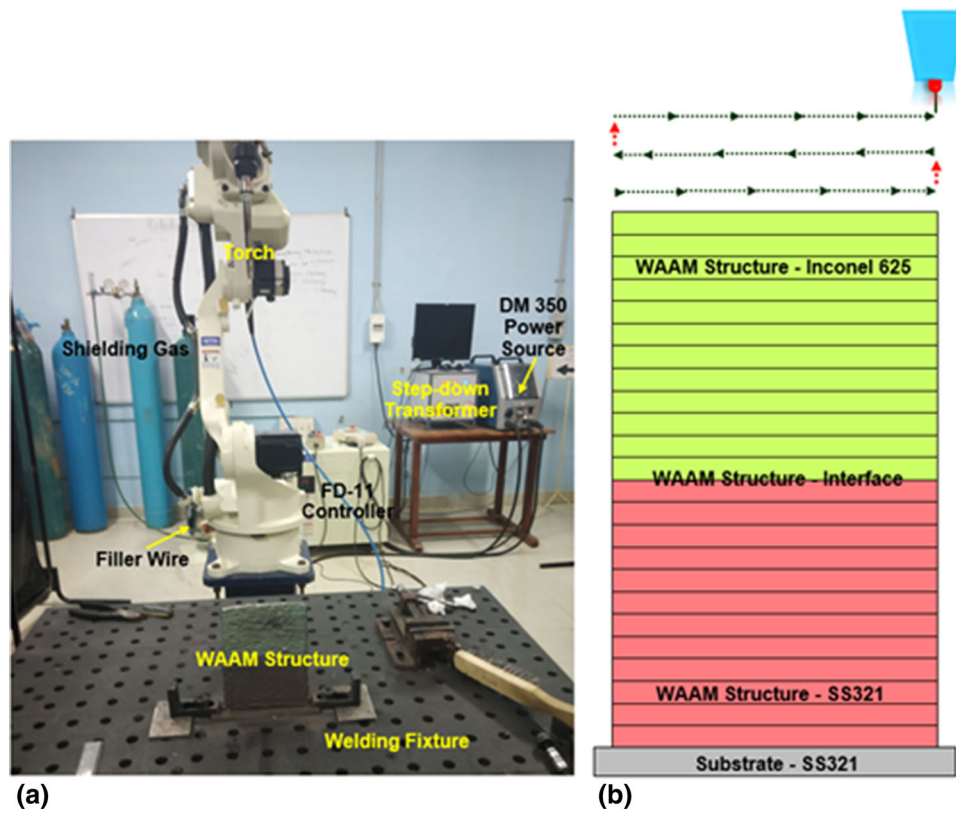


**Fig. 1** The WAAM system for fabricating FGM (a) Robotic welding system, (b) schematic illustration of FGM

**Table 1** Chemical composition of the filler wires (wt.%)

Filler wire/element	Si	C	S	Mn	Ni	Cr	Fe	Cu	Nb + Ta	Mo	Ti	P
ER321	0.50	0.049	0.020	1.47	9.10	19.05	68.67	0.15	...	0.46	0.50	0.024
ER625	0.44	0.1	0.001	0.50	63.67	22.26	0.50	0.23	3.70	8.40	0.40	0.015

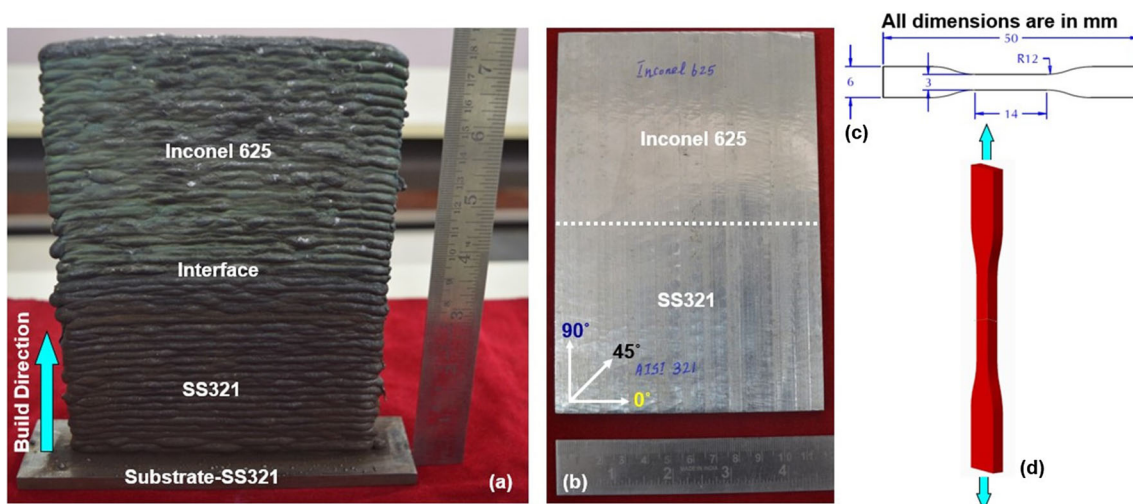


**Fig. 2** As-produced FGM: (a, b) before and after machining, (c) sample size for tensile test and (d) tensile loading of specimen

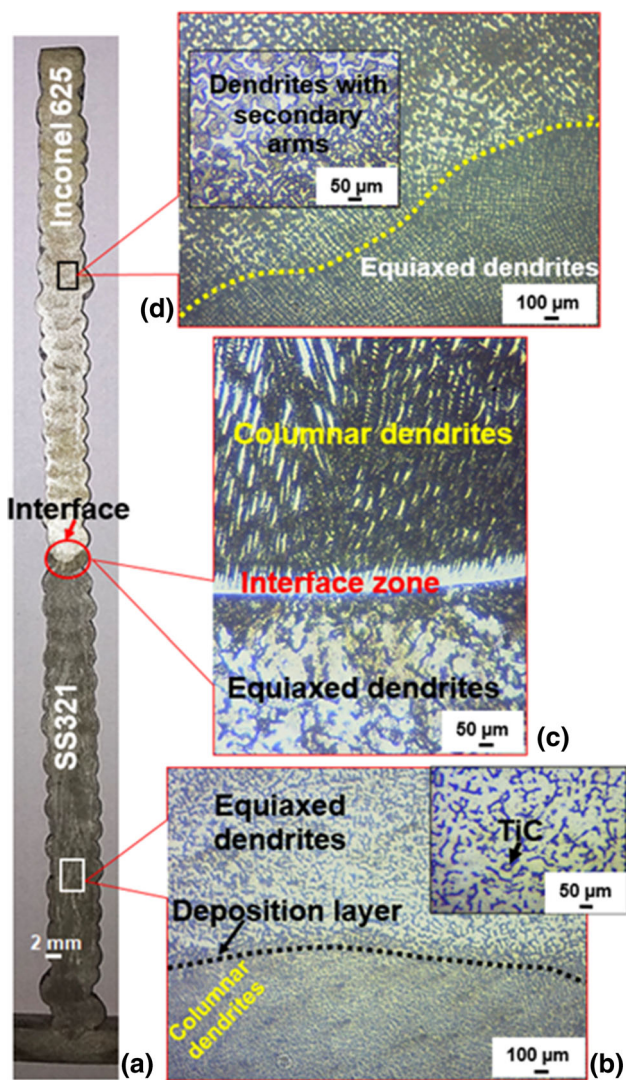


**Fig. 3** Macrostructure and optical micrographs of as-produced FGM: (a) overall structure, (b) SS321 side, (c) bi-metallic interface and (d) Inconel 625 side

Carroll et al. (Ref 8) manufactured SS304L/Inconel625 FGM without apparent composition and calculated the stability of the material by thermodynamic simulation. He observed that the micrometer-sized particles rich in Mo and Nb caused cracks in the upper layers where the composition of 304L was 82% by volume. Tungsten-copper FGM widely used in plasma-facing components was produced by selective laser melting and discussed the microstructure, interfacial defects, and bonding strength (Ref 17). Tey et al. (Ref 18) additively manufactured FGM of SS316L to Ti-6Al-4V with an interlayer of copper-nickel-silicium alloy-Hovadur K220. The microstructural examination revealed the existence of Cu-rich matrix at the Copper-stainless steel interface which comprises of a non-homogenous SS bands. The titanium-copper interface was characterized with  $\alpha'$ -Ti phase within the brittle matrix of  $Ti_2Cu + \beta-Ti$ , which is attributed to the non-homogeneous mixing within the melt pool.

The recent advancements on WAAM technology to produce FGM are successful and promising for critical applications. Ahsan et al. (Ref 19) manufactured FGM of austenitic stainless steel (ER316LSi) and low carbon steel (ER70S-6) with WAAM

process and evaluated the effect of heat treatment on the microstructural evolution and mechanical properties. The tensile properties of the heat-treated samples improved significantly compared to the as-produced FGM. Duplex stainless steel (ER2209) and mild steel (ER70S-6) were employed to manufacture FGM marine riser and the corrosion performance in marine environment was examined (Ref 14). Kannan et al. (Ref 20) fabricated an FGM of Hastelloy C-276 and stainless steel 904L via WAAM process and systematically examined the microstructures and mechanical properties. The existence of p phases was noticed and the FGM tensile specimens failed in the stainless steel region with comparable tensile strength.

To the best of our knowledge, many studies have been carried out on the dissimilar weldments of SS321 and Inconel 625 with other grades. Incoloy 800H and SS321 were joined with GTAW process using two different filler wires, Inconel 82 and Inconel 617 (Ref 21). Microstructural analysis confirmed the existence of precipitates such as TiC and TiN in the austenitic matrix and obtained comparable mechanical properties with Inconel 617 weldment. Dissimilar weldments of SS904L and Inconel 625 were used in key industries such as oil and gas extraction, marine, powerplants and nuclear water reactors. The excellent weldability and versatile corrosion performance of these alloys motivated to understand the mechanical properties and microstructural evolution of WAAM processed FGM. However, only few works have been focused in the fabrication and characterization of FGM via WAAM process. In this research, ER321 filler wire was first deposited on the SS321 substrate followed by ER625 layers. Also, it attempts to give an insight into the microstructural features and mechanical integrity of the SS321/Inconel 625 FGM.

## 2. Experimental Details

Consumable material of ER321 and ER625 was used for WAAM process. The deposition was fulfilled in OTC Daihen welding robot system. As presented in Fig. 1(a), SS321 substrate was used to deposit layers of ER321 first and ER625 was deposited over ER321. Based on the trial and error experiments, the welding parameters used were: 160 A current, 16.8 V, 30 cm/min deposition speed and 2.83 and 2.99 kg/h deposition rate for SS321 and Inconel 625, respectively. Figure 1 shows the WAAM system for producing FGM. The arc was scanned in a zig-zag pattern. The weld bead width was  $\sim 8$  mm and height of each layer was  $\sim 3$  mm. Hence an offset of 3.5 mm was set in the z direction between each layer to maintain the contact tip-to-work distance. Argon-100% shielding gas employed for depositing ER625 (30 layers), while at Argon-98% +  $CO_2$ -20% was used for ER321 (30 layers). The FGM plate was milled to attain uniform thickness and to reduce the delineations during deposition. The size of the as-deposited wall before machining ( $180 \times 135 \times 8$  mm) and after machining ( $170 \times 115 \times 4$  mm). Table 1 reports the chemical composition of the consumables.

The as-produced FGM before and after machining is shown in Fig. 2(a), (b). Metallographic specimens were prepared along the building direction from SS321, bi-metallic interface and Inconel 625 regions. The samples were prepared in accordance with ASTM E3-11(2017) standard. The microstructural features were captured using Olympus metallurgical microscope and Zeiss field emission-scanning electron microscope (SEM).



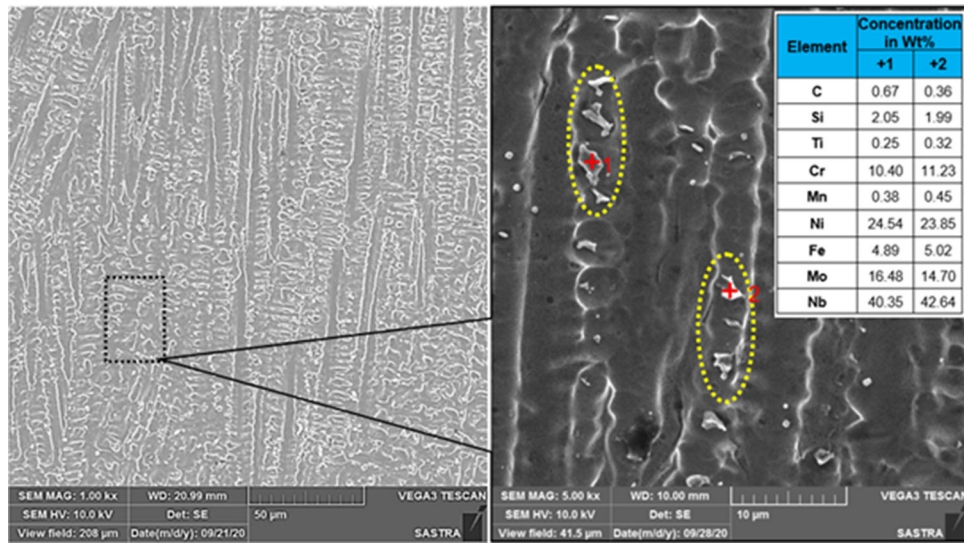


**Fig. 4** SEM micrograph highlighting the presence of precipitates in the Inconel 625 side

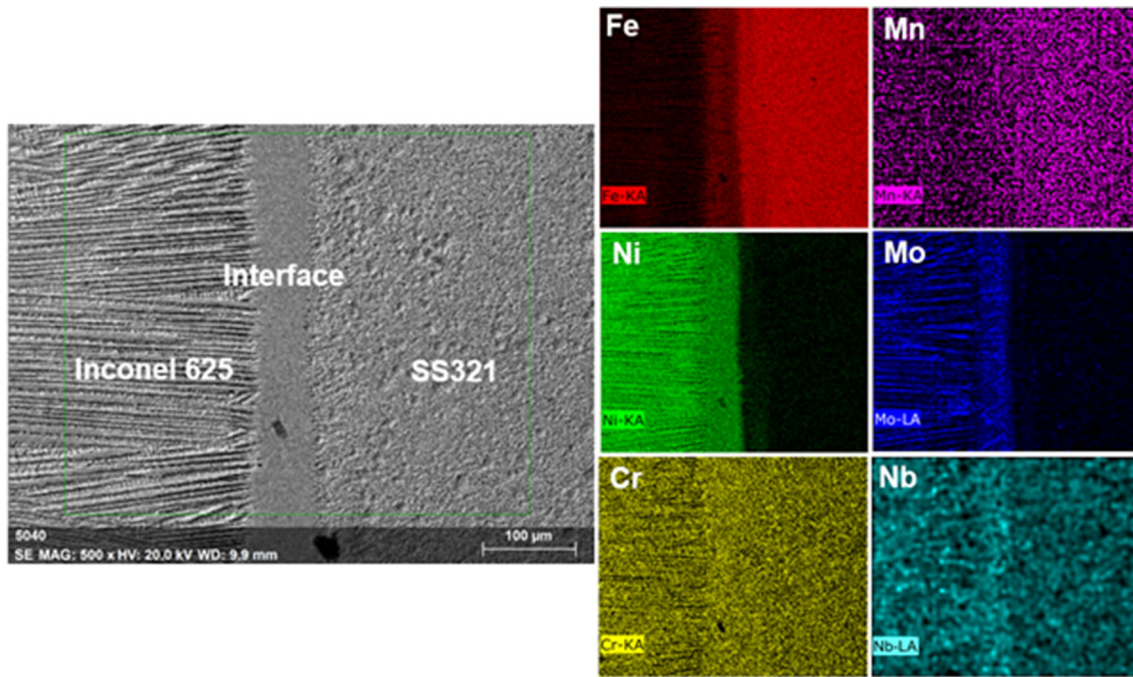


**Fig. 5** SEM micrograph with EDS elemental maps at the bi-metallic interface

Energy-dispersive x-ray spectroscopy (EDS) area scan, line scan, and elemental mapping were carried out to evaluate concentration of elements at various regions. EBSD examination was conducted using Fei Quanta 200 HV SEM with EBSD detector to analyze the crystallographic information. The specimen size of the sample is shown in Fig. 2(c). The tensile test was conducted on an Instron universal testing machine using a cross head speed of 1 mm/min following ASTM E8/E8M-16a e1 standard procedures. Micro-hardness measurements were performed from SS321 to Inconel 625 using Wilson Hardness 402 MVD system in accordance with ASTM E384-17. The test force was set to 500 gf and a dwell time of 10s. Three indentations were performed at each point and the

average values were recorded. SEM fractographs were captured to reveal the fracture morphology of the failed tensile samples.

### 3. Results and Discussion

Figure 3 reveals the macrograph and microstructural characteristics of the as-produced FGM at various locations. The macrostructure (Fig. 3a) revealed the strong metallurgical bond at the bimetallic interface and was free from defects. The bright regions were austenite, and the dark ferrite areas resembled to grain boundaries similar to those of AISI 321 (Fig. 3b) and Gusarova et al. (Ref 22) observed identical characteristics while

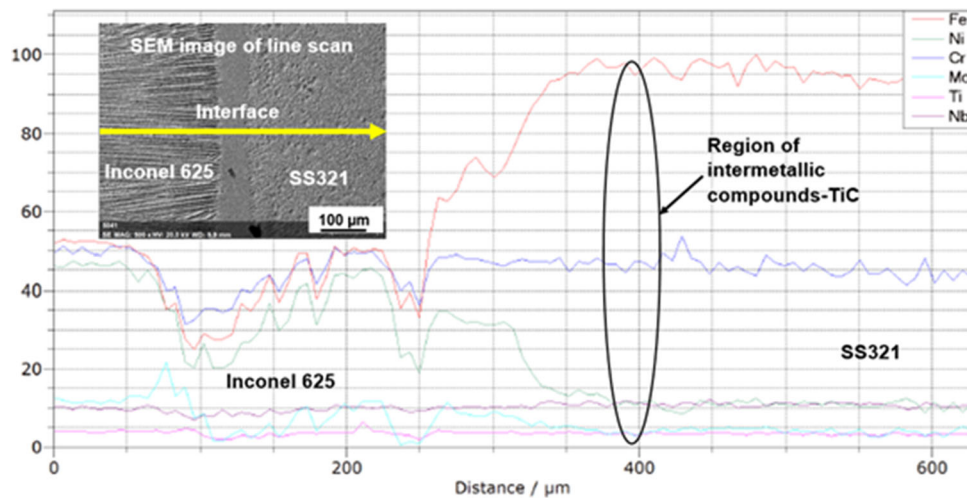


**Fig. 6** EDS line scan results at the bi-metallic interface

depositing SS321. The SS region is mainly composed of austenite (FCC) with a small volume of ferrite (BCC), due to the presence of residual  $\delta$ -ferrite. The ferrite amount ranged from 3.7 to 6.3 FN in the SS321 region. The structure is predominantly dendritic (equiaxed and columnar) and the growth direction deviates as the height of the SS321 region increases.

The dendritic spacing increased from bottom to top as a result of the different heating and cooling cycles experienced along the direction of build-up during WAAM process (Ref 23). The complex cyclic thermal cycles during the WAAM process exhibit a higher temperature gradient resulting in epitaxial growth of the columnar dendrites through the molten pool boundaries along the building direction by forming bands of remelted layers (Ref 24). The nucleation and growth of equiaxed dendrites during successive layer deposition restricts the growth of columnar dendrites and thereby aids the formation of equiaxed dendrites, which results in the transition of columnar to equiaxed grains (Ref 25). This phenomenon has been widely noticed during the fabrication of various materials via additive manufacturing techniques (Ref 26). Figure 3(c) represents the microstructure at the SS321/Inconel 625 interface and is similar to the FGM fabricated with 304L/Inconel 625 (Ref 27). The bonding between two alloys was excellent and clearly the partially melted zone-PMZ (bright zone in Fig. 3c) observed in the SS321 region does not affect the integrity of the FGM. The microstructure in the first layer of Inconel 625 (Fig. 3c) over SS321 was dendritic. The successive layers of Inconel 625 developed a coarser microstructure (Fig. 3d) as a result of the high temperature encountered during the deposition of previous layers. The Inconel 625 region consists of a comparable morphology with melt pools that accommodate coarse and fine equiaxed grains as well as columnar dendrites as reported by Yangfan et al. (Ref 28).

Figure 4 shows the SEM micrograph highlighting the presence of precipitates in the Inconel 625 layers. These precipitates were not continuous and are observed in between the dendrite arms. Also, from the EDS point analysis (points + 1 and + 2) it is confirmed that the concentration of Mo and Nb is higher and is in the range of 14.70-16.48% and 40.35-42.64%, respectively. The wt.% of Nb and Mo reveals the existence of laves phase and is generally observed in welded

Inconel 625 layers (Ref 29). Laves phases have HCP structure and exist in the form of  $(\text{Ni, Cr, Fe})_2(\text{Nb, Ti and Mo})$  (Ref 30). These results are in line with the previous results (Ref 31).

Figure 5 reveals the EDS elemental mapping results across the interface region. During fusion welding of dissimilar alloys, the PMZ is prone to liquation cracks (Ref 27, 32) and no such defect was observed in the bi-metallic interface. In addition, the existence of TiC was observed in the SS321 region, while Nb and Mo segregated in the Inconel 625 side. EDS line scan result (Fig. 6) confirmed the existence of TiC precipitates, while laves phase was observed with the help of SEM micrograph and EDS analysis. The presence of TiC avoids weld decay in SS321. EDS area scan results at SS321, bi-metallic interface and Inconel 625 side are presented in Fig. 7. It is noted that elemental migration occurred in the bi-metallic interface and is evident from Table 2. The increase in the wt.% of Mo, Nb, Fe and decrease in the concentration of Ni confirmed the existence of precipitates.

The EBSD results including inverse pole figure (IPF) map (Fig. 8a), grain boundary map (Fig. 8b), pole figure (Fig. 8c) and fraction of misorientation angle (Fig. 8d) on the SS321 region are presented. The distribution of grain size revealed the existence of smaller grains and most of these grains are fenced by large columnar dendrites. The color variation in the IPF map corresponds to austenitic grains in regard to crystal structure and each color represents set of Euler angles (Ref 33). The IPF map highlights that the preferred grain growth in the SS321 is in the  $\langle 001 \rangle$  and  $\langle 101 \rangle$  orientation (green and red color) along the build direction. The pole figure also confirms that the strong texture in the  $\langle 001 \rangle$  orientation with a small fraction of ferrite. The fraction of high angle grain boundaries (HABs) is higher compared to low angle grain boundaries (LABs). The 38% of misorientation angles are below  $15^\circ$  while 62% HABs are above  $15^\circ$ . This trend is attributed to the remelting of previous layers during deposition. The arrow mark indicates the building direction. The LABs concentration influences the yield strength slightly because of their mobility in regard to HABs. Generally, fraction of HABs was higher than 95% in the wrought counter parts (Ref 34).

The EBSD results in the Inconel 625 side revealed the existence of smaller grains and larger columnar dendrites as presented in Fig. 9. The microstructure was mainly austenitic



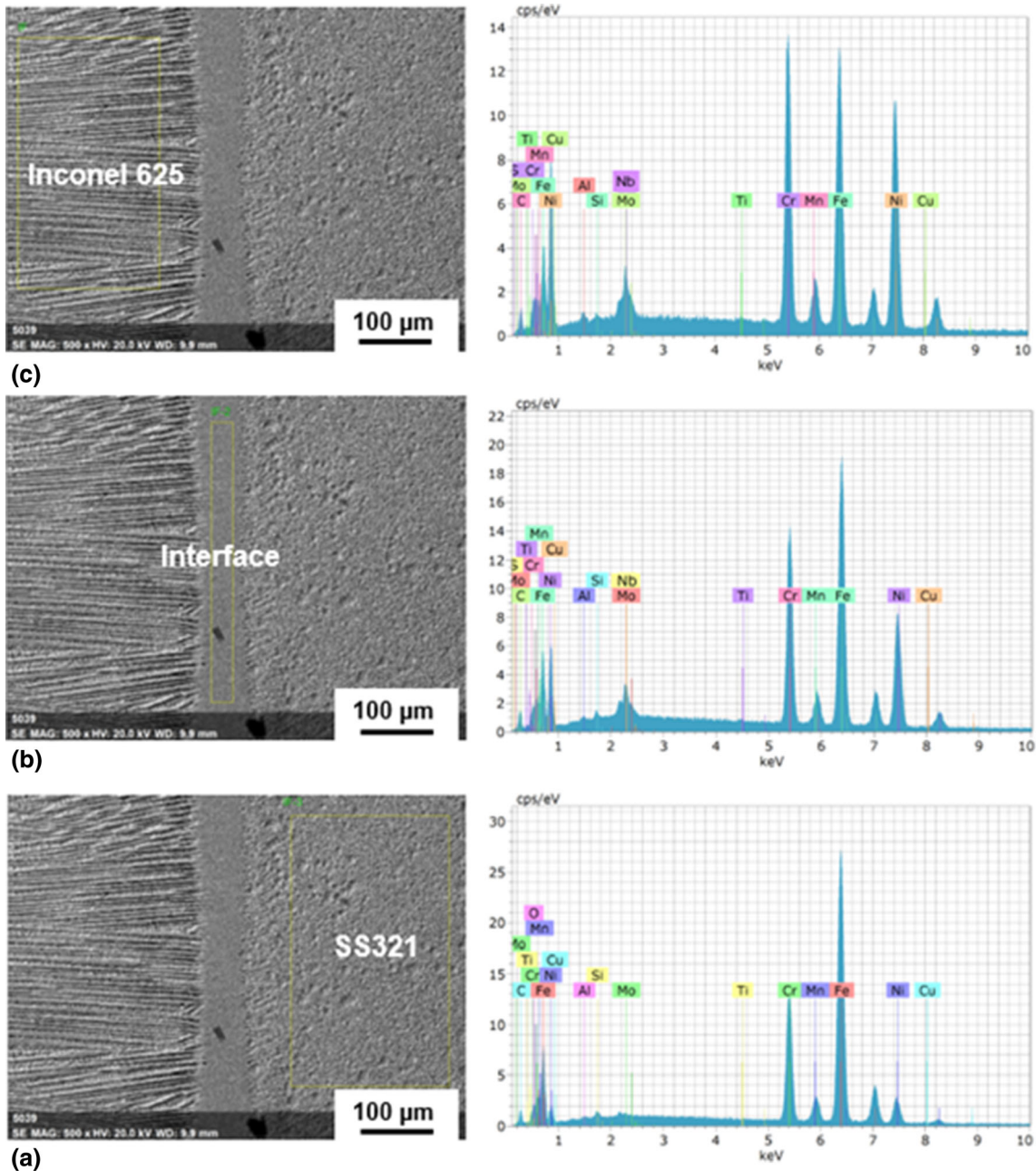


Fig. 7 EDS area scan results at various locations of the FGM: (a) SS321 side, (b) bi-metallic interface and (c) Inconel 625 side

Table 2 EDS analysis results at various regions of FGM

Element/zone	SS321	Interface	Inconel 625
Fe	64.79	34.90	15.28
Ni	9.50	28.41	24.93
Cr	17.78	29.32	20.62
Mn	1.53	0.96	0.45
Mo	0.07	9.65	14.70
Nb	0.79	5.60	19.62
Ti	0.24	0.62	0.32

(Fig. 9a). The variation in the grain size is corroborated to the difference in cooling rate and temperature within a single layer. The re-melted region undergoes sudden solidification by

forming fine grains while the rest of the layer forms columnar dendrites. The slower solidification phenomenon aided in the formation of columnar grains. The fraction of HABs and LABs (Fig. 9b) was 48% and 52%, respectively. The preferred orientation for grain growth (yellow and red color) is  $\langle 001 \rangle$  and this is along the build-up direction. Similar type of texture was observed in the previous work (Ref 31). The pole figure (Fig. 9c) along the building direction revealed monocrystalline strong texture and is evident from IPF map. Secondary precipitates were not detected in the EBSD examination and the presence of laves phase was confirmed with EDS analysis. HABs dominate in the Inconel 625 sample (Fig. 9d).

From the published literature, it is noticed that Inconel 625 comprises of an  $\gamma$ -austenitic (Ni) face-centered cubic-solid solution in which the secondary intermetallic precipitates like  $\delta$

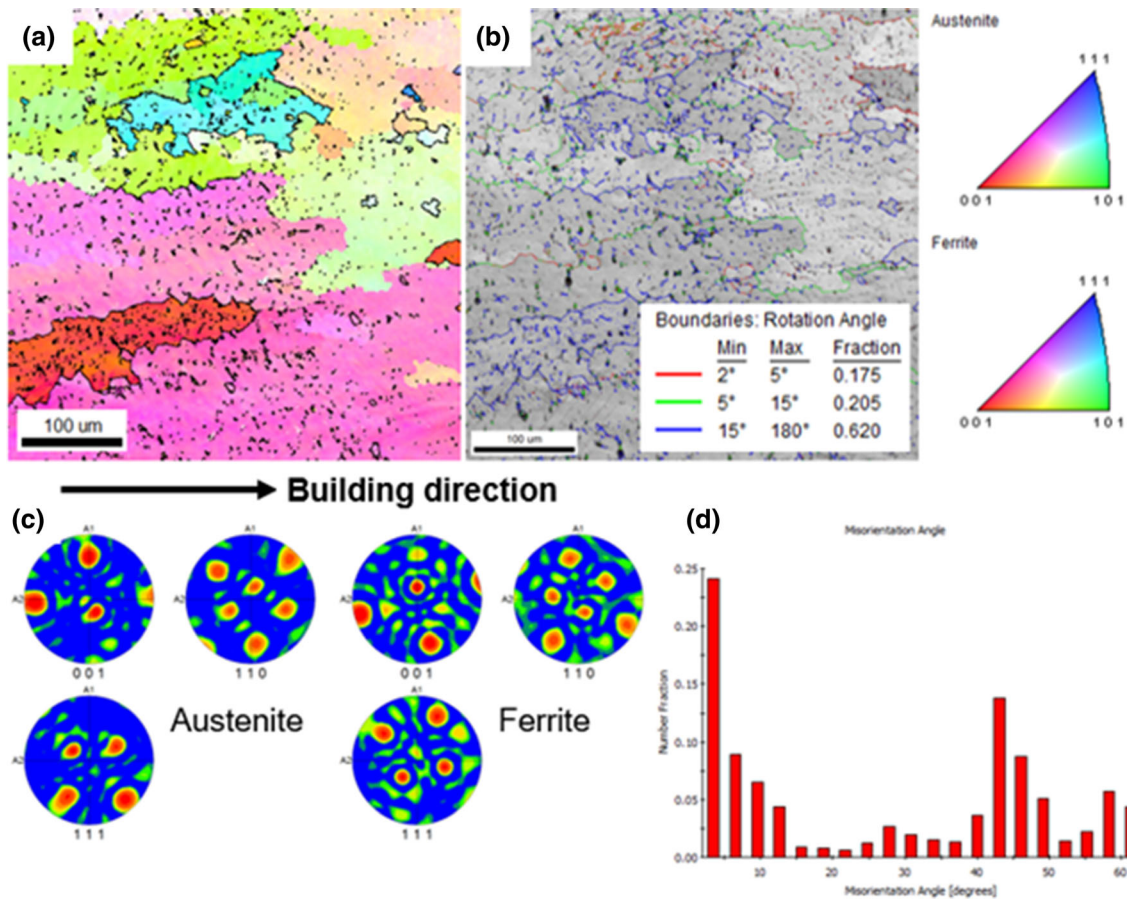


**Fig. 8** EBSD examination outcomes on the SS321 side: (a) IPF map, (b) grain boundary map, (c) pole figure and (d) misorientation angle distribution

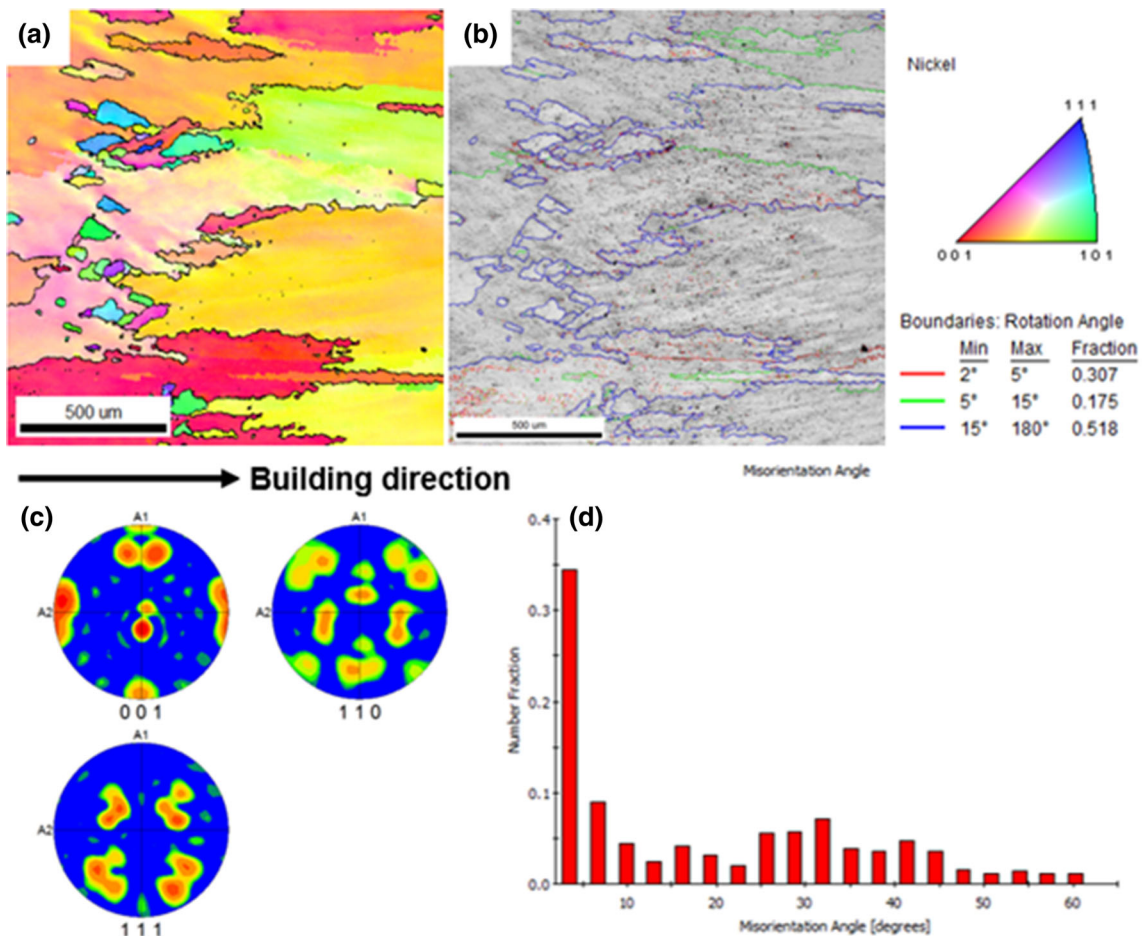
and  $\gamma''$  are distributed uniformly within the equiaxed grains or along the grain boundaries (Ref 35, 36, 37). These microstructural characteristics provide better mechanical properties for wrought ones. The higher cooling rate during the WAAM process influences the texture and grain morphology of the printed components. It is noticed that most of the grains were elongated parallel to build direction. Significant dendritic growth was observed with columnar, fine, and cell-form dendrites. In addition, secondary intermetallic precipitates segregated within the  $\gamma$ -Ni matrix to form laves phase and these elongated dendrites do not improve the mechanical properties significantly. These microstructural features can increase the hardness and YS values, while the reduction in UTS is noticed. The mechanical properties of as-printed Inconel 625 can be enhanced with proper annealing or heat treatment techniques compared to wrought alloy.

Figure 10 presents the EBSD results of the SS321/Inconel 625 bi-metallic interface with IPF map, grain boundary map, image quality map, pole figure and misorientation angle concentration. The microstructure was mainly dendritic, and the interface can be easily identified (Fig. 10b, c). However, no discontinuity was observed in the crystallographic growth at the interface and large elongated columnar dendrites were noticed. Identical results were reported during the deposition of Inconel 718 over SS316 (Ref 38). Pole figures of austenite and ferrite confirm the dissolution of Fe in the interface region (Fig. 10d). The 38.30% of misorientation angles are below 15° while 61.7% HABs are above 15° (Fig. 10e). The increase in the

wt.% of Fe promotes the segregation of Nb and Mo. Since both the alloys have an austenitic-FCC structure, and the preferred growth direction is in the  $\langle 001 \rangle$  orientation while the bi-metallic interface illustrated no discontinuity in grain growth. From the grain boundary maps, it is noticed that most of the grain boundaries in the SS321 and interface regions were preferentially HABs with a misorientation of 25°–60°, while the fraction of HABs and LABs are almost equal in Inconel 625 region. The higher bead height during the WAAM process compared to powder-based additive manufacturing techniques probably resulted in coarse dendritic structures with a higher fraction of misorientation angles. The higher fraction of HABs in the SS321 is attributed to the rapid solidification which occurs due to dendrites formation and accumulates misorientation during the WAAM process. The distribution of HABs noticed in the Inconel 625 region is identical to the previous study by Pleass and Jothi (Ref 39), where the existence of HABs could strongly influence the mechanical properties with easy cracking tendency. The size of the elongated dendrites was higher than 400  $\mu\text{m}$  and increased with increasing deposition height. These larger grains increased the percent of elongation in the Inconel 625 specimens.

Figure 11 and Table 3 show the tensile properties such as yield strength-YS, tensile strength-UTS, and Elongation for different types of samples sliced from the FGM in various orientations in relation to build direction. The YS and UTS of SS321 specimens at all orientations were higher than the wrought counterparts and are attributed to the dendritic





**Fig. 9** EBSD examination outcomes on the Inconel 625 side: (a) IPF map, (b) grain boundary map, (c) pole figure and (d) misorientation angle distribution

microstructure. The minimum YS, UTS, and elongation of AISI 321 according to ASTM A240/A240M-20a standard is 205 MPa, 515 MPa, and 40%, respectively (Ref 40). Also, the minimum YS, UTS, and elongation of Inconel 625 in accordance with ASTM B443-19 standard were 276 MPa, 690 MPa, and 30%, respectively (Ref 41). The YS and elongation of Inconel 625 were comparable with cast ones, while the YS was higher in all directions (Ref 42). The UTS and YS of SS321 specimens in the as-produced FGM were higher than the wrought counterparts, while the elongation reduced drastically due to the higher fraction of ferrite resulting in higher hardness.

The dendritic microstructure with secondary precipitates like laves phase influenced the tensile strength of Inconel 625. The YS and UTS interface sample was better than the SS321 and fractured in the weaker SS321 region away from the interface. The tensile properties obtained in this work for Inconel 625 are comparable with the tensile properties of WAAM processed Inconel 625 in as-deposited condition as reported by Yangfan et al. (Ref 28). The tensile properties were significantly influenced by the dendritic microstructure, precipitation, and the elements which aid the solid solution strengthening mechanism.

The percent of elongation was lower in the bi-material interface sample compared to SS321 and Inconel 625. Similar kind of results was attained by the earlier investigations on

additive manufactured structures (Ref 31, 38, 43). The tensile samples demonstrated anisotropy and are attributed to the varying microstructure and preferential growth of austenitic grains along the build direction. Also, the upward growth of the coarse columnar dendrites results in anisotropic behavior, i.e., crystallographic anisotropy.

The hardness values across the FGM in as-produced condition is plotted in Fig. 12. The hardness values in the SS321 and Inconel 625 were better than the wrought alloys. On cooling, the microstructure changed to austenite, leaving a small amount of ferrite (< 7%), which increased the micro-hardness of the first few layers deposited and gradually decreased from bottom to top (226 HV to 195 HV) in the SS321 region and this is attributed to complex cyclic thermal history (Ref 23). With the deposition of Inconel 625 over the SS321, the hardness value increased at the interface (291.6 HV) due to the dissolution of more wt.% of Cr, Nb, Fe, and Mo. This is due to the solid solution strengthening phenomenon which improved the hardness value. Identical results have been reported with the weldments and additive manufactured structures of stainless steels and nickel-based super alloys (Ref 44, 45). In the current work, hardness values had a steep increase within the 1 mm range from the interface. The micro-hardness plot shows a clear decrease in microhardness (272.3 HV to 236.6 HV) in the Inconel 625 region with increasing build height and the results were comparable to the previous



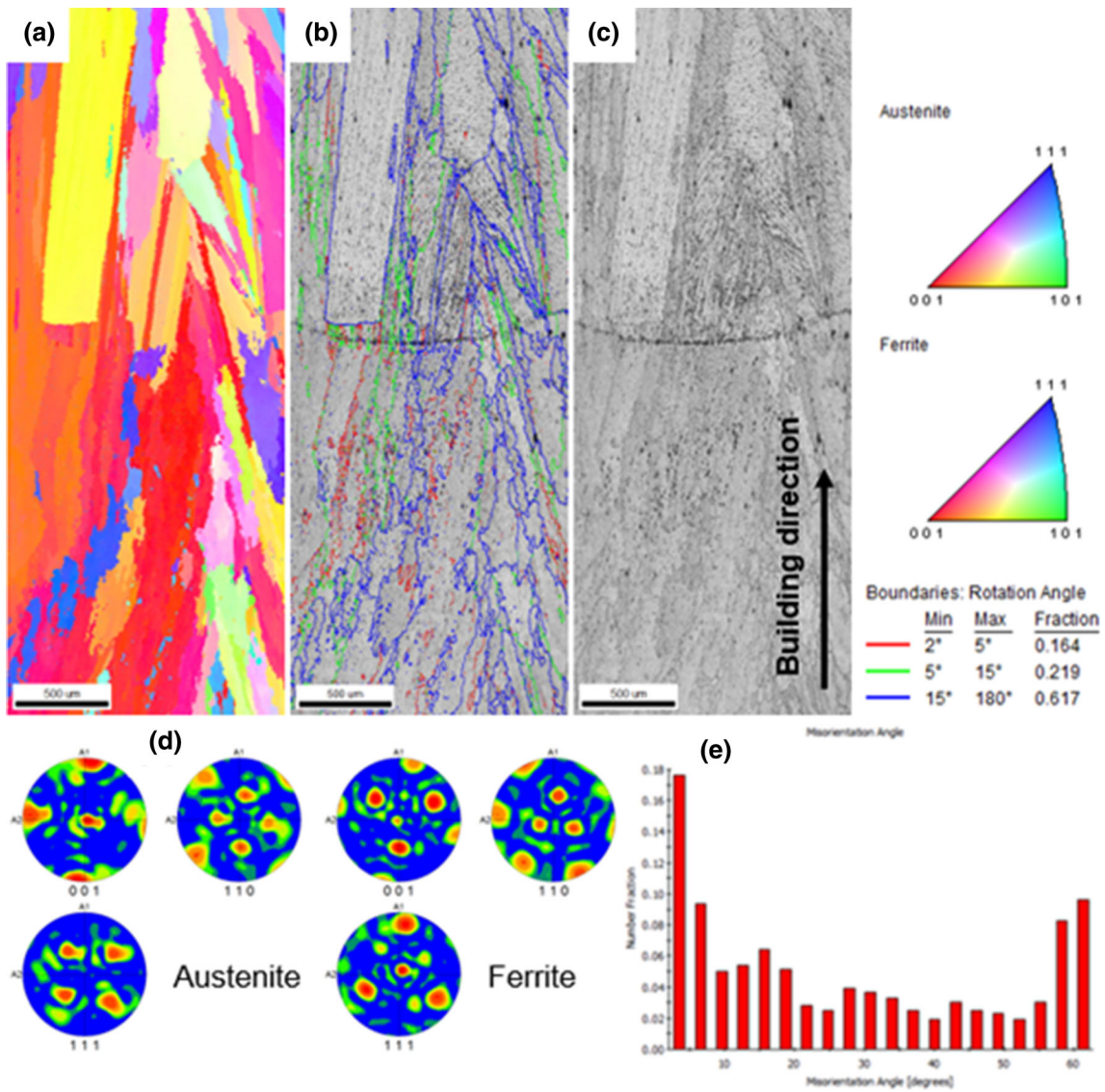


Fig. 10 EBSD examination outcomes on the bi-metallic interface: (a) IPF map, (b) grain boundary map, (c) pole figure and (d) misorientation angle distribution

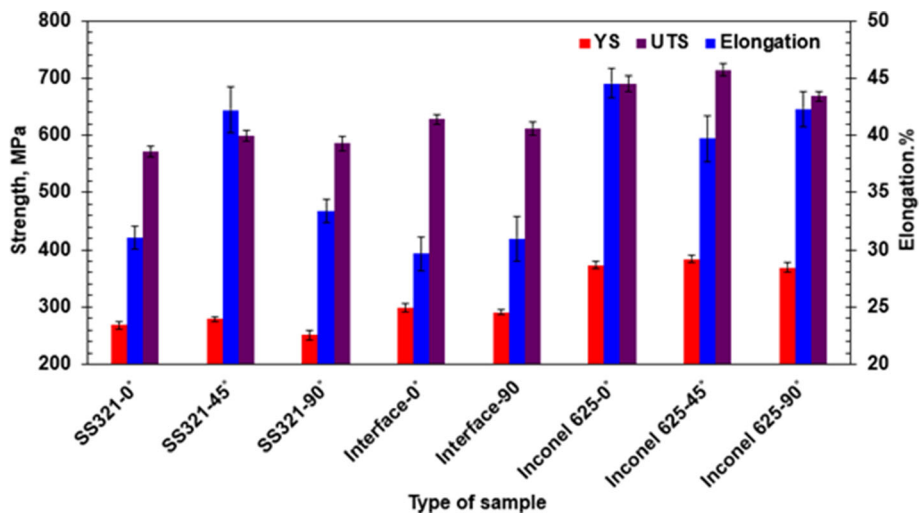
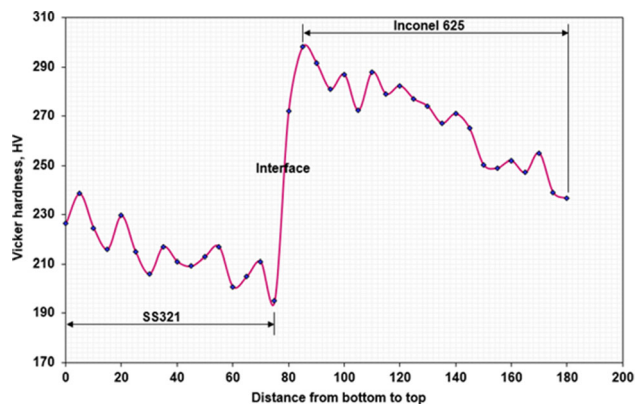


Fig. 11 Tensile properties of the various samples prepared from as-produced FGM

**Table 3 Tensile test results at various regions of the as-produced FGM**

Sample type		Yield Strength, MPa	Tensile Strength, MPa	Elongation, %
SS321	0°	268 ± 6	572 ± 10	31.02 ± 1.0
	45°	279 ± 4	599 ± 9	42.21 ± 2.0
	90°	251 ± 9	586 ± 13	33.37 ± 1.0
	ASTM A240/A240M-20a	205	515	40
Interface	0°	298 ± 7	628 ± 8	29.67 ± 1.5
	90	291 ± 5	612 ± 11	30.96 ± 2.0
IN625	0°	373 ± 6	690 ± 13	44.55 ± 1.2
	45°	384 ± 7	714 ± 10	39.71 ± 2.0
	90°	369 ± 8	668 ± 8	42.29 ± 1.5
	ASTM B443-19	276	690	30

**Fig. 12** Micro-hardness variation in FGM from bottom of the SS321 to top of the Inconel 625

research as a result of the varying dendrite spacing and existence of secondary precipitates (Ref 28).

The FGM samples from different locations had enough plastic deformation prior to fracture, indicating that the FGM samples failed in ductile mode (Ref 16, 37). The fractured surfaces consist of fine dimples, micro voids, and secondary particles as shown in Fig. 13. The sample from the interface at 90° fractured in the SS321 region and confirms the strong bonding at the bi-metallic interface. The fracture location points out that the weakest region is SS321 in the FGM sample (Fig. 13-IV), which means that WAAM based FGM fabrication is successful. The micro morphology of the Inconel 625 (Fig. 13-III a, b) sample depicted the presence of micro-fissures with dimples and rich phases of Mo and Nb were observed (Ref 28, 31). The micro voids nucleated and propagated along the secondary precipitates to fracture the test specimen during plastic deformation. The micro-cracks form and propagate in the stress-concentrated area, which leads to breakage. The bi-

metallic interface sample at 0° orientation shows the presence of fracture morphologies of the both the alloys (Fig. 13-II a, b).

#### 4. Conclusions

In the present work, FGM of SS321 and Inconel 625 were fabricated using WAAM process. The subsequent microstructural features and mechanical integrity were examined, and following inferences could be drawn:

- The WAAM-based fabrication was successfully demonstrated to form multi-material structures without any fissures and cracks.
- The microstructural characteristics varied along the build direction, with equiaxed and columnar dendrites in the SS321 region while the Inconel 625 layers comprised of fine, columnar and cell-form dendrites with the existence of secondary arms and precipitates.
- SS321 microstructure was mainly austenitic with significant fraction of δ-ferrite within the austenite matrix, while Inconel 625 was fully austenitic with the presence of laves phase.
- EBSD examination confirmed that the preferred grain growth direction was <001> orientation in the interface without discontinuity in grain growth because of the identical crystal structure-FCC.
- EDS analysis confirmed the migration of alloying elements between the two alloys and laves phase was noticed in the interdendritic regions of Inconel 625 layers.
- The tensile properties such as YS, UTS, and elongation of the FGM samples were better for SS321 and comparable for Inconel 625 than that of wrought alloys. Bi-metallic interface sample at 90° orientation fractured in the SS321 side away from the interface with better strength than SS321.



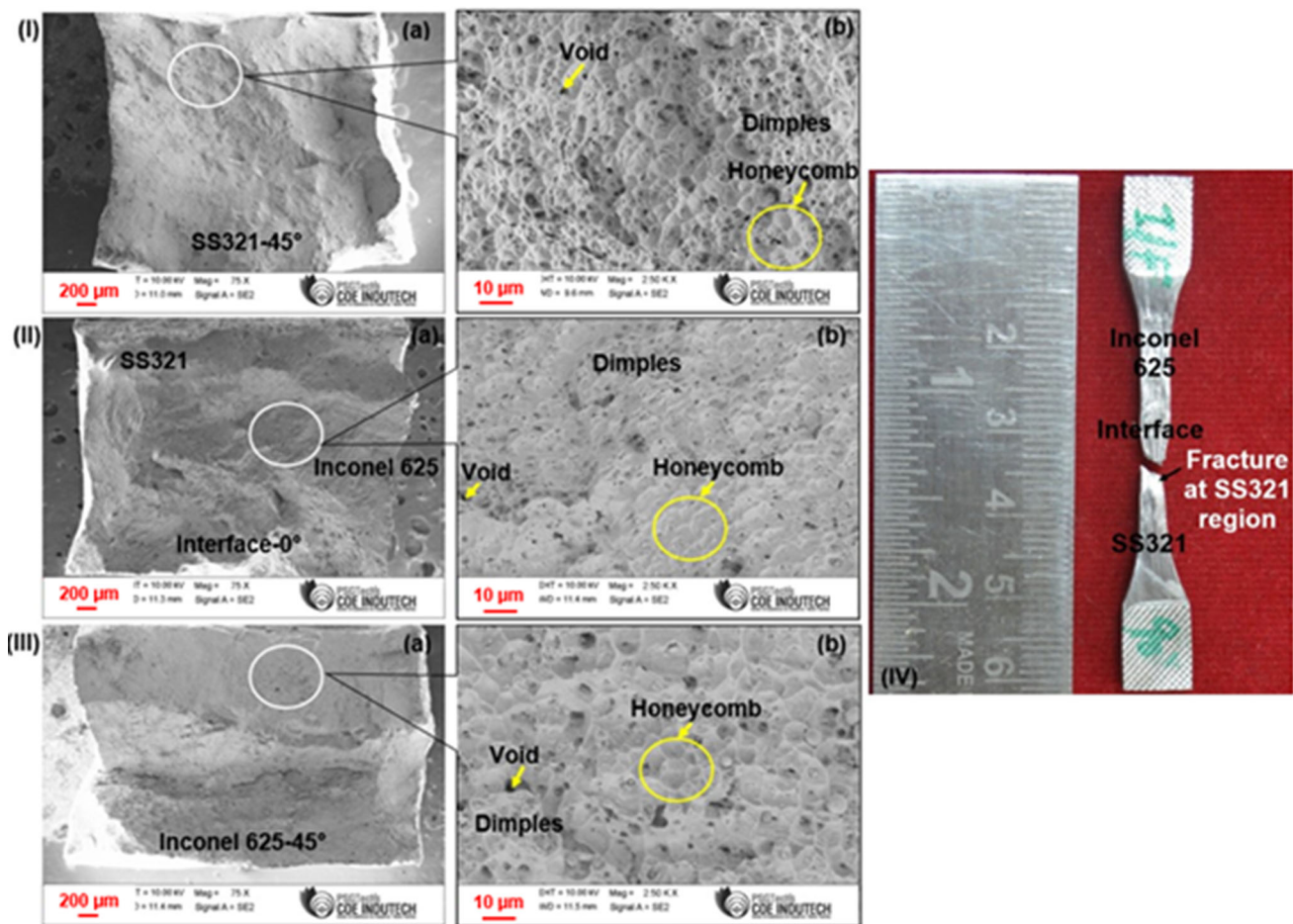


Fig. 13 SEM fractographs of various tensile samples and fractured interface 90° sample

- With the increasing deposition height, the micro-hardness values steadily decreased from bottom to interface and interface to top in the SS321 and Inconel 625 regions, respectively. The variation in micro-hardness is because of the microstructural variation along the built direction.
- The fractured locations were observed with dimples, voids, and micro-fissures. Rich precipitates of Nb and Mo were found in the Inconel 625 samples.

## References

1. R. Duraisamy, S. Mohan Kumar, A. Rajesh Kannan, N. Siva Shanmugam, K. Sankaranarayanan and M.R. Ramesh, Tribological Performance of Wire arc additive Manufactured 347 Austenitic Stainless Steel Under Unlubricated Conditions at Elevated Temperatures, *J. Manuf. Process.*, 2020, **56**, p 306–321
2. A.V. Nemani, M. Ghaffari and A. Nasiri, Comparison of Microstructural Characteristics and Mechanical Properties of Shipbuilding Steel Plates Fabricated by Conventional Rolling Versus Wire Arc Additive Manufacturing, *Addit. Manuf.*, 2020, **32**, p 101086
3. R. Pramod, S. MohanKumar, B. Girinath, A. RajeshKannan, N. PravinKumar and N. SivaShanmugam, Fabrication, Characterisation, and Finite Element Analysis of Cold Metal Transfer–Based Wire and Arc Additive-Manufactured Aluminium Alloy 4043 Cylinder, *Weld. World*, 2020, **64**, p 1905–1919
4. M. Bambach, I. Sizova, B. Sydow, S. Hemes and F. Meinersc, Hybrid Manufacturing of Components from Ti-6Al-4V by Metal Forming and Wire-Arc Additive Manufacturing, *J. Mater. Process. Technol.*, 2020, **283**, p 116689
5. I.F. Ituarte, N. Boddeti, V. Hassani, M.L. Dunn and D.W. Rosen, Design and Additive Manufacture of Functionally Graded Structures Based on Digital Materials, *Addit. Manuf.*, 2019, **30**, p 100839
6. B. Onuiké and A. Bandyopadhyay, Bond Strength Measurement for Additively Manufactured Inconel 718-GRCop84 Copper Alloy Bimetallic Joints, *Addit. Manuf.*, 2019, **27**, p 576–585
7. U. Reisgen, R. Sharma and L. Oster, Plasma Multiwire Technology with Alternating Wire Feed for Tailor-Made Material Properties in Wire and Arc Additive Manufacturing, *Metals*, 2019, **9**, p 745
8. B.E. Carroll, R.A. Otis, J.P. Borgonia, J. Suh, R.P. Dillon, A.A. Shapiro, D.C. Hofmann, Z.-K. Liu and A.M. Beese, Functionally Graded Material of 304L Stainless Steel and Inconel 625 Fabricated by Directed Energy Deposition: Characterization and Thermodynamic Modeling, *Acta Mater.*, 2016, **108**, p 46–54
9. M. Sireesha, S.K. Albert, V. Shankar and S. Sundaresan, A Comparative Evaluation of Welding Consumables for Dissimilar Welds Between 316LN Austenitic Stainless Steel and Alloy 800, *J. Nucl. Phys. Mater. Sci. Radiat. Appl.*, 2000, **279**, p 65–76
10. P. Varghese, E. Vetrivendan, M.K. Dash, S. Ningshen, M. Kamaraj and U. Kamachi Mudali, Weld Overlay Coating of Inconel 617 M on type 316 L stainless Steel by Cold Metal Transfer Process, *Surf. Coat. Technol.*, 2019, **357**, p 1004–1013
11. R.W. Hertzberg, R.P. Vinci and J.L. Hertzberg, *Deformation and Fracture Mechanics of Engineering Materials*, 5th ed. Wiley, Hoboken, 2013
12. D.E. Cooper, N. Blundell, S. Maggs and G.J. Gibbons, Additive layer Manufacture of Inconel 625 Metal Matrix Composites, Reinforcement Material Evaluation, *J. Mater. Process. Technol.*, 2013, **213**, p 2191–2200

13. V. Chaudhary, N.M.S. Kiran Kumar Yadav, S.A. Mantri, S. Dasari, A. Jagetia, R.V. Ramanujan and R. Banerjee, Additive Manufacturing of Functionally Graded Co-Fe and Ni-Fe Magnetic Materials, *J. Alloys Compd.*, 2020, **823**, p 153817
14. S. Chandrasekaran, S. Hari and M. Amirthalingam, Wire Arc Additive Manufacturing of Functionally Graded Material for Marine Risers, *Mater. Sci. Eng. A.*, 2020, **792**, p 139530
15. L.D. Bobbio, R.A. Otis, J.P. Borgonia, R.P. Dillon, A.A. Shapiro, Z.-K. Liu and A.M. Beese, Additive Manufacturing of a Functionally Graded Material From Ti-6Al-4V to Invar: Experimental Characterization and Thermodynamic Calculations, *Acta Mater.*, 2017, **127**, p 133–142
16. Bo. Chen, Su. Yi, Z. Xie, C. Tan and J. Feng, Development and characterization of 316L/Inconel625 functionally graded material fabricated by laser direct metal deposition, *Opt. Laser Technol.*, 2020, **123**, p 105916
17. C. Tan, K. Zhou and T. Kuang, Selective Laser Melting of Tungsten-Copper Functionally Graded Material, *Mater. Lett.*, 2019, **237**, p 328–331
18. C.F. Tey, X. Tan, S.L. Sing and W.Y. Yeong, Additive Manufacturing of Multiple Materials by Selective Laser Melting: Ti-Alloy to Stainless Steel Via a Cu-Alloy Interlayer, *Addit. Manuf.*, 2020, **31**, p 100970
19. M.R.U. Ahsan, A.N.M. Tanvir, G.-J. Seo, B. Bates, W. Hawkins, C. Lee, P.K. Liaw, M. Noakes, A. Nycz and D.B. Kim, Heat-Treatment Effects on a Bimetallic Additively-Manufactured Structure (BAMS) of the Low-Carbon Steel and Austenitic-Stainless Steel, *Addit. Manuf.*, 2020, **32**, p 101036
20. A. Rajesh Kannan, S. Mohan Kumar, R. Pramod, N. Pravin Kumar, N. Siva Shanmugam and Y. Palguna, Microstructure and Mechanical Properties of Wire Arc Additive Manufactured Bi-Metallic Structure, *Sci. Technol. Weld. Joining*, 2021, **26**, p 47–57
21. G. Sayiram and N. Arivazhagan, Microstructural Characterization of Dissimilar Welds Between Incoloy 800H and 321 Austenitic Stainless Steel, *Mater. Charact.*, 2015, **102**, p 180–188
22. A.V. Gusarova and E.S. Khoroshko, Influence of electron beam parameters on the structure and properties of 321 steel obtained by additive manufacturing, *AIP Conf. Proc.*, 2019, **2167**, p 020133
23. A. Rajesh Kannan, N. Siva Shanmugam, V. Rajkumar and M. Vishnukumar, Insight Into the Microstructural Features and Corrosion Properties of Wire Arc Additive Manufactured Super Duplex Stainless Steel (ER2594), *Mater. Lett.*, 2020, **270**, p 127680
24. J. Liu and A.C. To, Quantitative Texture Prediction of Epitaxial Columnar Grains in Additive Manufacturing Using Selective Laser Melting, *Addit. Manuf.*, 2017, **16**, p 58–64
25. D.R. Liu, S.H. Wang and W.T. Yan, Grain Structure Evolution in Transition-Mode Melting in Direct Energy Deposition, *Mater. Des.*, 2020, **194**, p 108919
26. F. Yan, W. Xiong and E. Faierson, Grain Structure Control of Additively Manufactured Metallic Materials, *Materials*, 2017, **10**, p 1260
27. S. Kou, *Welding Metallurgy*, Wiley, Hoboken, 2003
28. Y.F. Wang, X.Z. Chen and C.C. Su, Microstructure and Mechanical Properties of Inconel 625 Fabricated by Wire-Arc Additive Manufacturing, *Surf. Coat. Technol.*, 2019, **374**, p 116–123
29. M. Tümer, T. Mert and T. Karahan, Investigation of Microstructure, Mechanical, and Corrosion Behavior of Nickel-Based Alloy 625/ Duplex Stainless Steel UNS S32205 Dissimilar Weldments Using ERNiCrMo-3 Filler Metal, *Weld World*, 2020 <https://doi.org/10.1007/s40194-020-01011-0>
30. F. Hejripour and D.K. Aidun, Consumable Selection for Arc Welding Between Stainless Steel 410 and Inconel 718, *J. Mater. Process. Technol.*, 2017, **245**, p 287–299
31. M.R.U. Ahsan, X. Fan, G.-J. Seo, C. Ji, M. Noakes, A. Nycz, P.K. Liaw and D.B. Kim, Microstructures and mechanical behavior of the bimetallic additively-manufactured structure (BAMS) of austenitic stainless steel and Inconel, *J. Mater. Sci. Technol.*, 2021, **74**, p 176–188
32. S. Shakerin, A. Hadadzadeh, B.S. Amirkhiz, S. Shamsdini, J. Li and M. Mohammadi, Additive manufacturing of maraging steel-H13 bimetallics using laser powder bed fusion technique, *Addit. Manuf.*, 2019, **29**, p 100797
33. X. Chen, J. Li, X. Cheng, H. Wang and Z. Huang, Effect of heat treatment on microstructure, mechanical and corrosion properties of austenitic stainless steel 316L using arc additive manufacturing, *Mater. Sci. Eng. A.*, 2018, **715**, p 307–314
34. S. Mohan Kumar, S. Sankarapandian and N. Siva Shanmugam, Investigations on mechanical properties and microstructural examination of activated TIG-welded nuclear grade stainless steel, *J. Braz. Soc. Mech. Sci. Eng.*, 2020, **42**, p 292
35. M. Khler, Effect of the Elevated-Temperature-Precipitation in Alloy 625 on Properties and Microstructure, Paper Presented at Superalloys 718, 625, 706 and Various Derivatives, TMS, Pittsburgh, PA, USA (1991), pp. 363–374
36. M. Newell, K. Devendra, P.A. Jennings and N. D'Souza, Role of Dendrite Branching and Growth Kinetics in the Formation of Low Angle Boundaries in Ni–base Superalloys, *Mater. Sci. Eng. A.*, 2005, **412**, p 307–315
37. A. Rajesh Kannan, S. Mohan Kumar, N. Pravin Kumar, N. Siva Shanmugam, A.S. Vishnu and Y. Palguna, Process-Microstructural Features for Tailoring Fatigue Strength of Wire Arc Additive Manufactured Functionally Graded Material of SS904L and Hastelloy C-276, *Mater. Lett.*, 2020, **274**, p 127968
38. A. Hinojos, J. Mireles, A. Reichardt, P. Frigola, P. Hosemann, L.E. Murr and R.B. Wicker, Joining of Inconel 718 and 316 Stainless Steel Using Electron Beam Melting Additive Manufacturing Technology, *Mater. Des.*, 2016, **94**, p 17–27
39. C. Pleass and S. Jothi, Influence of Powder Characteristics and Additive Manufacturing Process Parameters on the Microstructure and Mechanical Behaviour of Inconel 625 Fabricated by Selective Laser Melting, *Addit. Manuf.*, 2018, **24**, p 419–431
40. ASTM International, A240/A240M-20a Standard Specification for Chromium and Chromium-Nickel Stainless Steel Plate, Sheet, and Strip for Pressure Vessels and for General Applications. West Conshohocken, PA; ASTM International, 2020. [https://doi.org/10.1520/A0240\\_A0240M-20A](https://doi.org/10.1520/A0240_A0240M-20A)
41. ASTM International, B443-19 Standard Specification for Nickel-Chromium-Molybdenum-Columbium Alloy and Nickel-Chromium-Molybdenum-Silicon Alloy Plate, Sheet, and Strip. West Conshohocken, PA; ASTM International, 2019. <https://doi.org/10.1520/B0443-19>
42. F. Xu et al., Microstructural Evolution and Mechanical Properties of Inconel 625 alloy During Pulsed Plasma Arc Deposition Process, *J. Mater. Sci. Technol.*, 2013, **29**, p 480–488
43. K. Shah, I.U. Haq, A. Khan, S.A. Shah, M. Khan and A.J. Pinkerton, Parametric Study of Development of Inconel-Steel Functionally Graded Materials by Laser Direct Metal Deposition, *Mater. Des.*, 2014, **54**, p 531–538
44. J. Rodriguez, K. Hofer, A. Haelsig and P. Mayr, Functionally Graded SS 316L to Ni-Based Structures Produced by 3D Plasma Metal Deposition, *Metals.*, 2019, **9**, p 620
45. H. Naffakh, M. Shamanian and F. Ashrafzadeh, Microstructural Evolutions in Dissimilar Welds Between AISI 310 Austenitic Stainless Steel and Inconel 657, *J. Mater. Sci.*, 2010, **45**, p 2564–2573

**Publisher's Note** Springer Nature remains neutral with regard to jurisdictional claims in published maps and institutional affiliations.